JOURNAL OF PROPULSION AND POWER
Vol. 26, No. 6, November–December 2010

Spray Generated by an Airblast Atomizer Under Elevated Ambient Pressures

Mouldi Chrigui,* Ilia V. Roisman,† Feras Z. Batarseh,‡ Amsini Sadiki,§ and Cam Tropea¶
Technical University of Darmstadt, 64287 Darmstadt, Germany

DOI: 10.2514/1.47833

The objective of this work is to study a spray generated by an airblast atomizer at elevated ambient pressures. The study includes the measurement of a typical spray's integral parameters (average drop diameter and average three-dimensional velocity vector of liquid and gas phases), numerical simulation of spray propagation, and models validation. The numerical study of the spray evolution was carried out using an accurate numerical spray module based on an Euler–Lagrange method accounting for drops evaporation. The experimental data were collected using the phase Doppler and particle image velocimetry techniques. The drop diameter and two velocity components were measured simultaneously using two-dimensional phase Doppler system. These data were used as initial conditions for the numerical simulations (data in the neighborhood of the atomizer exit) and for the validation of the numerical method (data on the spray parameters measured at various distances from the atomizer). The droplet diameter and spray velocity are shown to be influenced by the enhancing of the ambient chamber pressure.

Nomenclature

B_M	=	Spalding mass transfer number
B_T	=	Spalding heat transfer number
$C_{\varepsilon,3}^{k-\varepsilon}$	=	constant model for the turbulence modulation
C_w	=	drag coefficient
c_p	=	specific heat capacity by constant pressure, $\mathrm{J/(kg \cdot K)}$
D_m	=	diffusion term in scalar transport equation, $\mathrm{m^2 s^{-1}}$
D_p	=	droplet diameter, m
$\mathbf{F}/F_i$	=	force, N
$\mathbf{g}/g_i$	=	gravity acceleration vector/Cartesian components, $\mathrm{m/s^2}$
h_v	=	latent heat of vaporization, KJ/Kg
k	=	turbulent kinetic energy, $\mathrm{m^2 s^{-2}}$
L_E	=	turbulent length scale, m
Le	=	Lewis number
$\dot{m}_{p,v}$	=	droplet evaporation rate, Kg/s
N_p	=	number of real droplets represented by one numerical parcel
Pr	=	Prandtl number
$\dot{Q}$	=	heat flux rate penetrating into the droplet interior, J/s
Re	=	Reynolds number
Re_p	=	droplet Reynolds number
Sc	=	Schmidt number
Sh	=	Sherwood number
St	=	Stokes number
$S_{\psi,p,s}$	=	source term of the variable ψ for a nonevaporating droplet, ψ dependent
$S_{\psi,p,v}$	=	source term of the variable ψ due to evaporation, ψ dependent
T	=	temperature, K
T_L	=	Lagrangian integral time scale, s
t	=	times
$\mathbf{u}/(u, v, w)$	=	velocity vector/Cartesian components, m/s
$\mathbf{u}_p/(u_p, v_p, w_p)$	=	droplet velocity vector/Cartesian components, m/s
u', v', w'	=	gas phase velocity fluctuation components, m/s
u'_p, v'_p, w'_p	=	disperse phase velocity fluctuation components, m/s
$V_{i,j,k}$	=	volume of the cell ijk, $\mathrm{m^3}$
ν/ν_t	=	kinematic molecular/turbulent viscosity, $\mathrm{m^2/s}$
y	=	vapor mass fraction
α_p	=	droplet volume fraction
ε	=	turbulent kinetic energy dissipation rate, $\mathrm{m^2/s^3}$
μ/μ_t	=	dynamic molecular/turbulent viscosity, $\mathrm{Kg/(m \cdot s)}$
ρ	=	density of mass, $\mathrm{Kg/m^3}$
$\upsilon_{s,\mathrm{eq}}$	=	molar mass fraction

I. Introduction

MANY practical combustion systems, such as internal combustion and gas turbine engines, involve vaporization and spray combustion in high-pressure environments. In particular, combustion in modern gas turbine engines fired with liquid fuels is strongly influenced by the fuel preparation process. This includes the atomization of the liquid fuel, the dispersion and evaporation of the droplets in a fuel spray and the mixing of fuel vapor and air. The atomization of a liquid into small droplets in the form of a spray is an important process in industrial and combustion systems. A larger surface area is produced by forming droplets, thus reducing the liquid vaporization time. In liquid fuel combustion applications this results in better mixing and an increase in the time available for complete combustion [1].

Airblast atomizers have often been used due to the significant reduction in soot formation and exhaust smoke that they achieve in gas turbine engines. A comprehensive review of airblast atomizers can be found in [2,3]. The parameters of the spray generated by an airblast atomizer (for example, typical drop size and velocity) depend

Received 26 October 2009; revision received 25 May 2010; accepted for publication 16 June 2010.

*Doctor, Institute of Energy and Power Plant Technology, Department of Mechanical Engineering; mchrigui@ekt.tu-darmstadt.de.

†Associate Professor, Chair of Fluid Mechanics and Aerodynamics, Department of Mechanical Engineering; roisman@sla.tu-darmstadt.de.

‡Doctor, Chair of Fluid Mechanics and Aerodynamics, Department of Mechanical Engineering; f.batarseh@sla.tu-darmstadt.de.

§Professor, Institute of Energy and Power Plant Technology, Department of Mechanical Engineering; sadiki@ekt.tu-darmstadt.de.

¶Professor, Chair of Fluid Mechanics and Aerodynamics, Department of Mechanical Engineering; tropea@sla.tu-darmstadt.de.

on many factors: viscosity of the liquid and its flow rate, density, surface tension and air velocity. To date, many investigations have been performed to better understand the atomization process. Usually such studies lead to a formulation of empirical relations for spray integral or average parameters as functions of operation conditions of a specific atomizer. Such results are not universal since the atomizer design and geometry influence significantly the spray parameters. Many of the previous investigations were performed to develop new atomizers and study the atomization outcome under laboratory conditions [4,5]. One main problem is the prediction of the average drop diameter in the spray. This parameter is usually an unknown factor in a numerical simulation of the atomization process or other prediction tools.

Liquid fuel injected into gas turbine or rocket combustors is rapidly atomized into clouds of vaporizing droplets that quickly ignite and burn. Detailed knowledge of fuel spray formation is required and characteristic drop size measurements are needed at the point of initial spray formation near the atomizer orifice to accurately describe the fuel spray combustion process [6].

Depending on application, the ambient gas into which sprays are injected can vary widely with pressure and temperature. This is especially true of liquid fuel-fired combustion systems. In diesel engines the pressure and temperature can reach critical and supercritical conditions. In gas turbine combustors, fuel sprays are injected into turbulent, swirling, recirculating streams of reacting gases [2]. Recent studies [7–9] were focused on droplet sauter mean diameter distributions in airblast sprays under elevated pressures and actual gas turbines conditions. They used a high air temperature to atomize kerosene liquid fuel in an airblast atomizer with prefilming.

Since the pressure in gas turbine combustion chambers has continuously risen in recent years, exceeding the critical pressure of the liquid fuel, this work aims to experimentally characterize the fuel spray properties generated by an airblast atomizer at various ambient pressures.

Computational fluid dynamics has become an important complement to experiments, providing early detailed information (at a moderate cost) of all the processes which strongly influence spray combustion [10–12]. A considerable body of work is available on a large range of nonreacting and reacting multiphase, gas–liquid flows or combusting sprays [13–15]. Diverse parameter studies have been carried out, however, there are relatively few results about the effects of pressure on the evolution of spray generated by an airblast atomizer and on the subsequent spray combustion [16,17]. Since the droplet temperature rises with increasing ambient pressure and temperature in a combustion chamber, the unsteady heating of the droplet must significantly affect the droplet evaporation process under high-pressure conditions, precluding the assumption of steady state evaporation.

The central aim of this numerical study is to use the spray module [10,18] to evaluate its ability to correctly describe the spray evolution process under different pressure conditions. This spray module includes the "uniform temperature evaporation model" [19]. An indirect aim of the numerical computations is to validate the experimental evaluation techniques employed. Both tasks are achieved by comparing experimental and numerical results.

In the following section, a description of the experimental work is given followed by some experimental results. The numerical method and procedure are then summarized. Before concluding the paper, numerical results compared with experimental data highlight the ability of the numerical spray module to describe the spray propagation under various pressure conditions.

II. Experimental Setup

A. Experimental Method

Experiments were performed in a pressure chamber with 4 cm-thick transparent, quartz windows allowing optical access to the spray (Fig. 1).

A hollow-cone, pressure-swirl nozzle [20] is used to produce the primary spray. Water is pumped to the hollow-cone nozzle by a reciprocating pump which is capable of maintaining a constant,

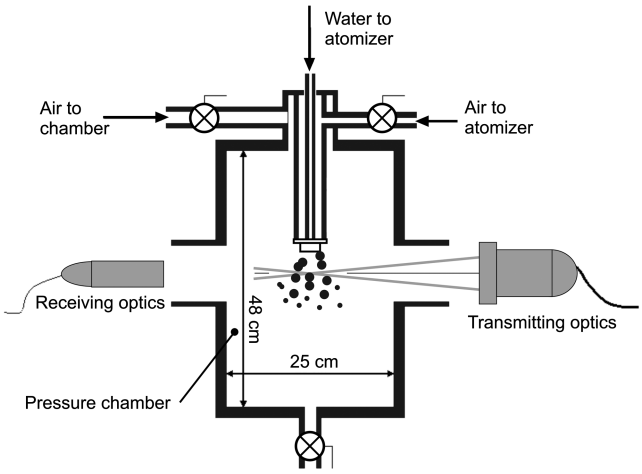

Fig. 1 Experimental setup.

controllable flow rate with relatively high pressure (up to 100 bar at maximum 3.24 l/hr). Compressed air is supplied to the chamber along two paths: the first path leads to the airblast atomizer (MTU-aero-engines nozzle) and assists the atomization; the second path leads directly to the chamber to regulate pressure in the chamber. The second airflow surrounds the atomizer outlet in an annular channel of 6-cm outer diameter. The measurements were performed over a 4 cm (−2 to 2 cm) diameter within the spray cone. The annular air curtain thus had no significant effect on the atomization process. The compressed air that moves through these paths comes from the same source and is then controlled by valves. The air in the path to the atomizer is measured by a mass flow transmitter device, based on the constant temperature difference principle. The use of the second, outer air path simplifies the control of the pressure inside the chamber while keeping a constant air flow rate to the atomizer.

An MTU atomizer was used to generate the hollow swirl spray. A detailed view of the MTU atomizer is shown in Fig. 2a. The primary

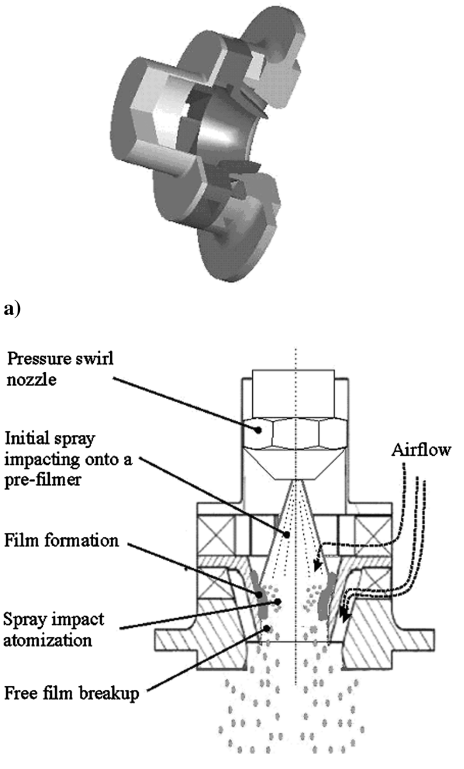

Fig. 2 Sketch of spray atomization: a) MTU atomizer and b) mechanisms of liquid breakup in the airblast atomizer.

drops first break up and partially follow the air flow. Next, a liquid film is formed on the prefilmer and ligaments are generated (due to the high air velocity) which break up into droplets, as schematically shown in Fig. 2b.

The phase Doppler instrument was used to characterize the spray: to measure the velocity and size distributions of the drops. Additionally, the particle image velocimetry (PIV) technique is used to generate averaged vector fields in the atomized spray and the air field.

Aerosol spray was used to visualize the air flow. There are no industrial aerosol generators able to create small aerosol particles in a high-pressure flow above 10 bar. An aerosol generator able to introduce aerosol particles in the high-pressure environment (up to 40 bar) has been designed and constructed. The generator consists of a: 1) pressure reducer connected with the high-pressure air line; 2) first chamber where the primary spray is created; and 3) second chamber where the primary spray droplets break up on the impacting plate and the large inertial drops are deposited and removed from the flow.

The aerosol is shown schematically in Fig. 3. Low viscosity vegetable oil is used as a working fluid in the aerosol generator.

B. Spray and Airflow Visualization

Spray visualization and PIV measurements were performed to better understand the spray and the process of its creation.

An example of PIV measurements is shown in Fig. 4. Figure 4a shows a single image of spray illuminated by a planar laser sheet. An example of an average velocity field obtained using the PIV technique is shown in Fig. 4b. The length and color of the arrows corresponds to the velocity magnitude. The spray droplets were used as markers for PIV, therefore, only the average spray velocity were measured. No explicit information about the air flow can be obtained from these measurements. Three main regions can be immediately recognized: 1) outer region 1 of relatively small velocity; 2) main spray region 2 of relatively high droplets velocity; and 3) inner region near the axis. The flow in this region is induced by the injected spray. This flow is nonstationary, turbulent. Some vortex structures are often created at the boundary between regions 2 and 3, leading to the typical fir-tree-like instantaneous shapes of the region 3 (Fig. 4a).

The slight asymmetry of the spray flow, seen in Fig. 4, may be originated from the nonperfectly assembled injector. Even by symmetrical geometry, small error during the construction prevails and make the spray injection slightly sloped. This asymmetry is transmitted to the flow that propagates toward the outlet. Moreover it may be accompanied with unsteady phenomena that augment its effect.

The motion of single droplets can be clearly seen in the images of the spray obtained using the high-speed video system. It could be expected that the motion of the relatively large water drops of diameters 15 to 50 μm is inertia dominated. However, the nearly straight drop trajectories typical of inertial drops were not observed. In fact, the droplets followed the swirl air flow. The shutter time in the image in Fig. 5 is relatively long, such that each drop is shown as a short line along the instantaneous drop trajectory. The spiral drop trajectories can be recognized even in the single image in Fig. 5. It is also clear that this phenomenon of capturing of droplets by a swirl air flow is only observed for very large values of the air-to-liquid mass ratio, typical to these experimental conditions. In this case, the momentum of the liquid fraction is small in comparison to the momentum of the air flow.

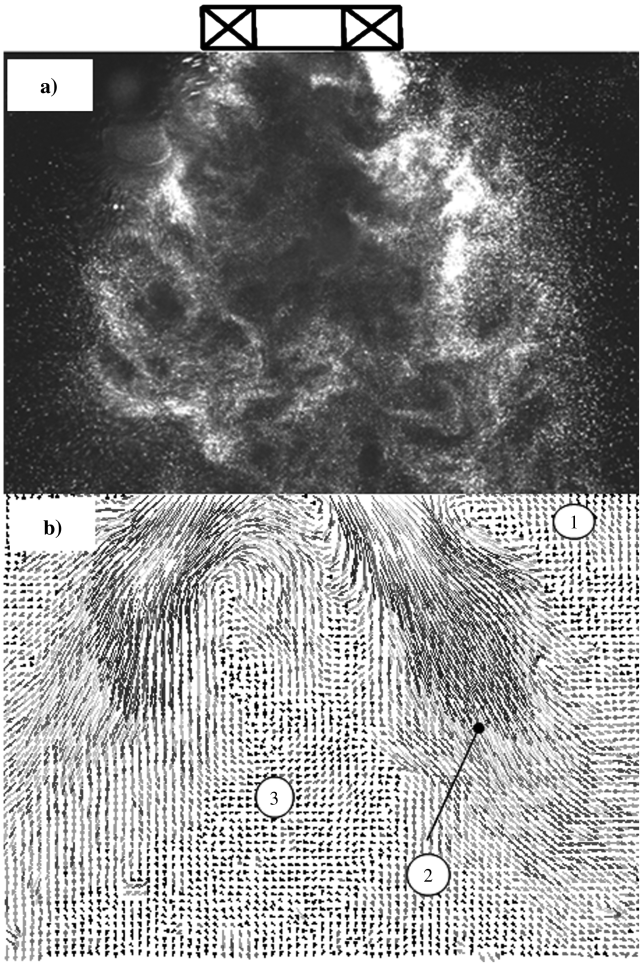

Fig. 4 Measured droplet characteristics obtained using a) planar laser sheet (inverse image) and b) PIV (spray vector plot).

The aerosol flow shown in Fig. 6 is illuminated in by a laser planar sheet in order to visualize airflow generated by the atomizer. Figures 6a–6c are plotted for increasing air volume flux, 22, 66 and 124 standard cubic meters per hour (SCMH), respectively. The two-phase flow homogeneity is clearly influenced. All the details of the flow can be seen in the images: spray cone, typical structure that looks similar to the fir tree form. These air flow structures can indicate the close connection of the instability of the spray propagation (seen in Fig. 4a) with the turbulent fluctuations of the swirl airflow. Moreover, the cone angle reduces as the flow rate of the air grows.

C. Spray Characterization Using the Phase Doppler Technique

Using the two-dimensional phase Doppler system, the drop diameter (D) and two velocity components, axial (U) and transverse

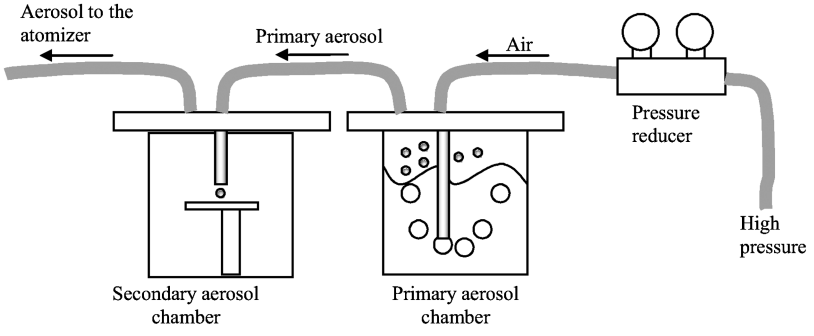

Fig. 3 High-pressure aerosol generator.

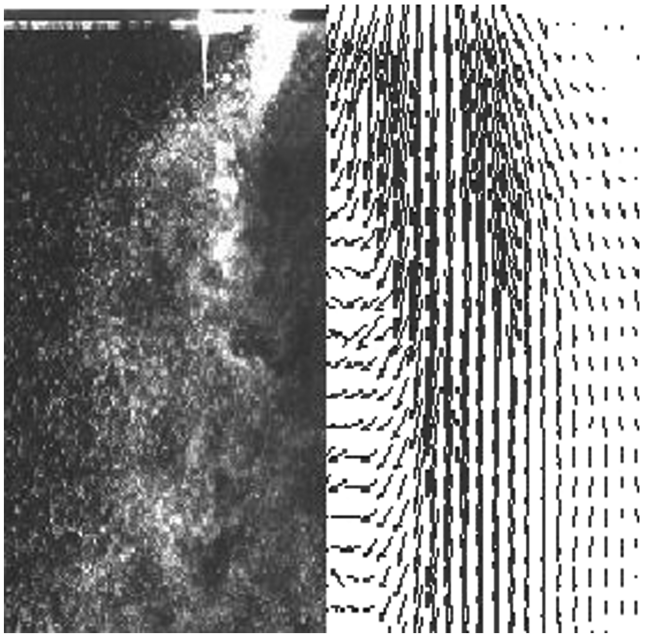

a)

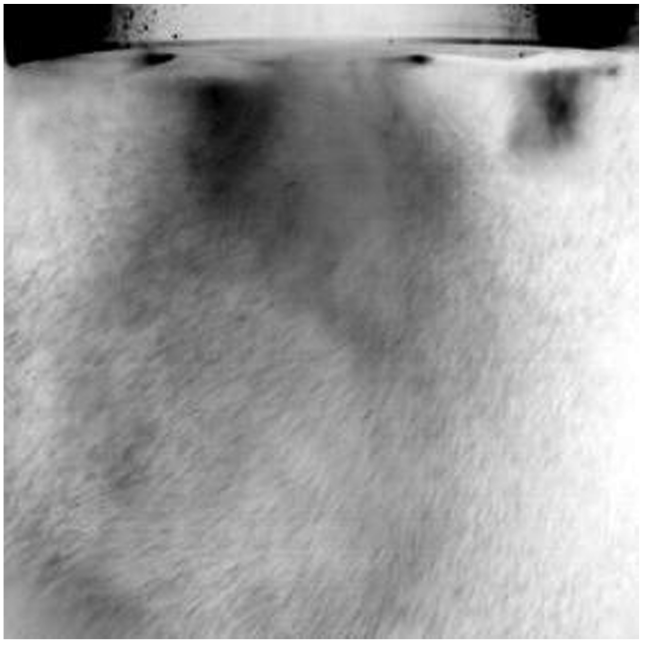

b)

Fig. 5 Atomized spray: qualitative image generated with high-speed video camera.

(V), can be measured. The transverse velocity coincides with the radial velocity (V) if the detection volume of the instrument is located in the plane y-z (see the sketch in Fig. 7). Here, the axis is directed towards the transmitting optics of the instrument, whereas the z axis is the axis of the spray. In the plane x-z, the measured transverse velocity component represents the azimuthal drop velocity, (W).

In the experiments, the drop diameter, and axial (U) and radial (V) drop velocities were measured simultaneously for each droplet in the plane y-z. The averaged azimuthal velocity component (W) was estimated separately using a different configuration of the phase Doppler instrument (measurements in the plane x-z). The method is based on the assumption of axial symmetry of the spray.

The phase Doppler data show that the ambient chamber pressure (called back pressure in some cases) affects the droplet diameter and the velocity of the spray, as shown in Fig. 8.

a)

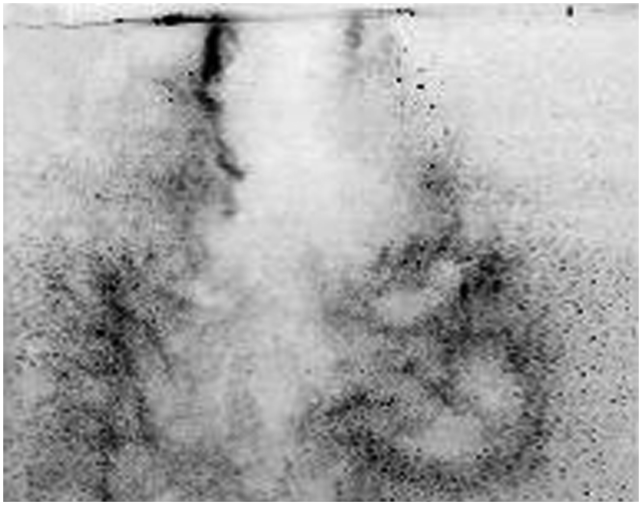

b)

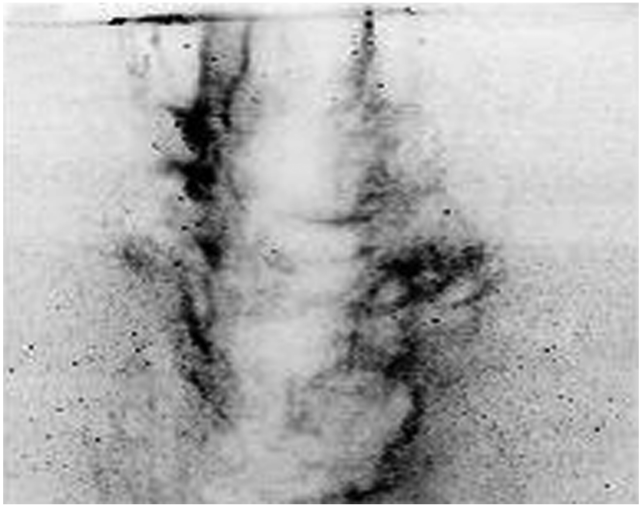

c)

Fig. 6 Inverse images of the aerosol flow following the air phase. The ambient pressure is 1 bar. The air flow rate is a) 22, b) 66, and c) 124 SCMH.

The axial spray velocity reaches a maximum at a radius of approximately 8 mm in the plane 11 mm downstream of the nozzle. This region corresponds to the main spray flow. Generally, three spray regions can be identified: main, outer and inner [21]. The

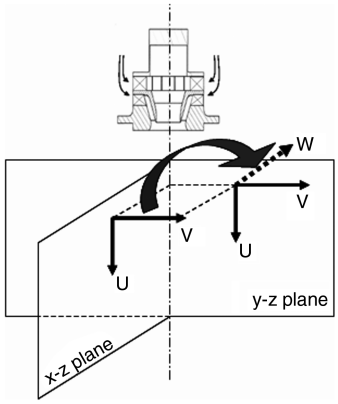

Fig. 7 Measurement planes in the pressure chamber.

velocity in the inner region can even be negative, indicating a vortex flow inside the spray cone. It should be noted that the spray in the inner region is rather sparse, which prolongs the collection of sufficient data required for a stable estimation of statistical spray parameters.

It is worth mentioning that achieving symmetrical profile for the spray properties, e.g., droplet diameter, velocity components or mass flux is a difficult task. This might be caused by the errors during the manufacturing. It is almost impossible to assemble the nozzle with all pipes absolutely in a symmetrical manner. Therefore, the construction errors of the experimental set up are mainly responsible for the asymmetry seen in the two-phase flow properties. Furthermore, the asymmetry in the disperse phase may be caused by the formation of droplet clusters which may appear due to resonance cases.

The change in the droplet diameter starts to be significant above 5 bar. The reason for this change is related to the mechanism that takes place inside the atomizer. There are two sources for droplets. The first one is the droplets generated directly as a result of the spray-impacting onto prefilmer, and the second source is the disintegration of the liquid film. To better understand the reason behind this increase in droplet diameter, the change in air velocity component first needs to be investigated, for example, as shown in Fig. 9.

It is clear that the velocity drops sharply at chamber pressures above 5 bar. This low velocity is responsible for the larger droplet diameters that are generated by the film break up.

Further quantitative data were gathered to build a comprehensive database to characterize the spray at various ambient pressures. The detailed report of the spray parameters can be found in [21].

The streamlines, isotherms and cross-sectional profiles of axial single-gas velocity as well as the two-component velocity vector of the carrier air have also been provided. Some exemplary quantitative results compared with numerical simulations are reported in this paper.

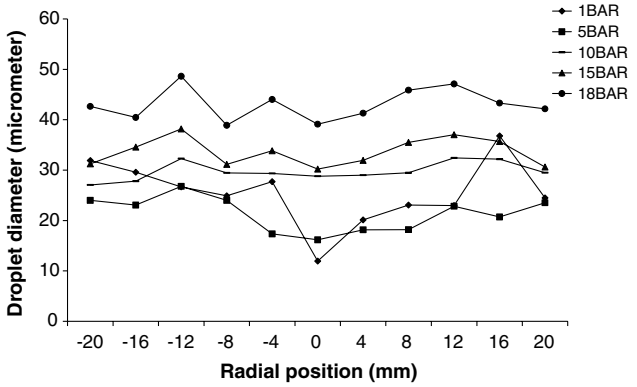

a)

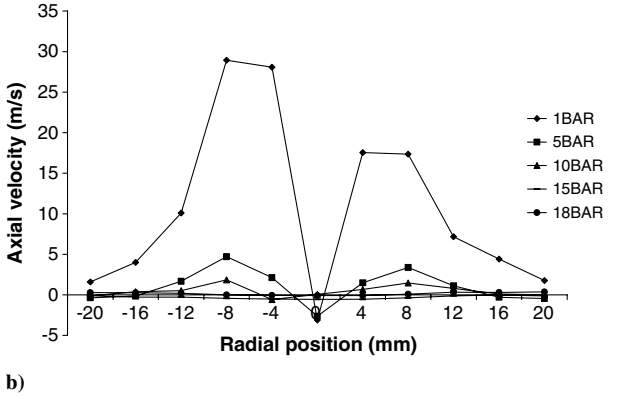

b)

Fig. 8 Droplet mean properties at different pressures and at 11 mm downstream of the nozzle: a) average drop diameter and b) axial drop velocity.

III. Numerical Approach

A. Carrier Phase

The numerical computations are performed using the Eulerian–Lagrangian approach. The carrier phase is considered the continuum phase and is described using the Reynolds-averaging method. For this purpose, the transport equations have been solved for mass conservation, momentum, concentration and temperature:

$$\frac{\partial \bar{\rho}}{\partial t} + \frac{\partial(\overline{\rho}\,\overline{u_i})}{\partial x_i} = \bar{S}_{1,p,v} \tag{1}$$

$$\frac{\partial(\overline{\rho}\,\overline{u_i})}{\partial t} + \frac{\partial(\overline{\rho}\,\overline{u_j}\,\overline{u_i})}{\partial x_j} = \bar{\rho} g_i - \frac{\partial \bar{p}}{\partial x_i} + \frac{\partial}{\partial x_j}\left(\bar{\rho}\Gamma_u \frac{\partial \bar{u}_i}{\partial x_j} - \overline{\rho\, u_i' u_j'}\right) + \bar{S}_{u_i,p,s} + \bar{S}_{u_i,p,v} \tag{2}$$

$$\frac{\partial(\overline{\rho}\,\overline{y})}{\partial t} + \frac{\partial(\overline{\rho}\,\overline{u_j}\,\overline{y})}{\partial x_j} = \frac{\partial}{\partial x_j}\left(\bar{\rho}\Gamma_y \frac{\partial \bar{y}}{\partial x_j} - \overline{\rho\, u_j' y'}\right) + \bar{S}_{y,p,s} + \bar{S}_{y,p,v} \tag{3}$$

$$\frac{\partial(\bar{\rho}\,\bar{T})}{\partial t} + \frac{\partial(\bar{\rho}\,\overline{u_j}\,\bar{T})}{\partial x_j} = \frac{\partial}{\partial x_j}\left(\bar{\rho}\Gamma_T \frac{\partial \bar{T}}{\partial x_j} - \bar{\rho}\,\overline{u_j' T'}\right) + \bar{S}_{T,p,s} + \bar{S}_{T,p,v} \tag{4}$$

For the turbulence description, the k-ε model, which was extended for two-phase flows, was considered:

$$\frac{\partial k}{\partial t} + \frac{\partial}{\partial x_i}(\bar{u}_i k) = \frac{\partial}{\partial x_i}\left(\frac{\nu_t}{Pr_k}\frac{\partial k}{\partial x_i}\right) - \overline{u_i' u_j'}\frac{\partial \bar{u}_j}{\partial x_i} - \varepsilon + \bar{S}_{k,p,s} + \bar{S}_{k,p,v} \tag{5}$$

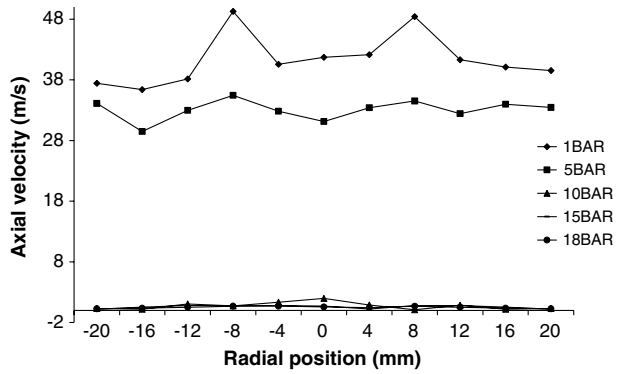

Fig. 9 Axial air velocity at different chamber pressures and at 11 mm downstream of the nozzle.

$$\frac{\partial \varepsilon}{\partial t} + \frac{\partial}{\partial x_i}(\bar{u}_i \varepsilon) = \frac{\partial}{\partial x_i}\left(\frac{\nu_t}{Pr_\varepsilon}\frac{\partial \varepsilon}{\partial x_i}\right) - C_{\varepsilon 1}\frac{\varepsilon}{k}\overline{u_i' u_j'}\frac{\partial \bar{u}_j}{\partial x_i} - C_{\varepsilon 2}\frac{\varepsilon^2}{k} + \bar{S}_{\varepsilon,p,s} + \bar{S}_{\varepsilon,p,v} \tag{6}$$

The variables Γ_u, Γ_y, Γ_T, ν_t, and Pr denote the diffusivity for momentum, vapor concentration and temperature, turbulent viscosity and the turbulent Prandtl number, respectively. The quantities $C_{\varepsilon 1}$ and $C_{\varepsilon 2}$ are model constants. The influence of the disperse phase on the fluid motion is treated as an extra force exerted on the carrier gas. Thus, the momentum transfer from the disperse phase to the carrier phase is included by adding a reaction force, which acts as a surface force on the droplet, to the Navier–Stokes equations. This model is known as the force coupling model or the particle-source-in-cell model proposed by Crowe [22]. The source terms $\bar{S}_{\psi,p,s}$ and $\bar{S}_{\psi,p,v}$ that characterize the direct interaction of mass, momentum, turbulence, energy and species between the droplets and the carrier gas are summarized in Table 1. The variable ψ represents the mean value of mass density, velocity components (u, v, w), temperature T, turbulent kinetic energy k, turbulent dissipation rate ε, and the mass fraction, respectively. $\bar{u}$, $\bar{v}$ and $\bar{w}$ are the mean gas phase (axial, tangential and transversal) velocity components. In Table 1, $\bar{u}_p$, $\bar{v}_p$ and $\bar{w}_p$ represent the three mean velocity components of the droplet. N_p is the number of real droplets represented by one numerical droplet. V_{ijk} is the cell volume. $\dot{Q}_i$ represents the heat flux into the droplet and g is the gravitation. $\dot{m}_p$ is the droplet's mass flow rate across a control volume per second. Δt is the Lagrangian integration time step. $\bar{S}_{u_i,p,v}$ represents the gas momentum flux emitted by the droplets during their vaporization. $\bar{S}_{1,p,v}$ is the mass released into the fluid by the droplets because of vaporization. The presence of droplets may be a source of turbulence dissipation or production in the carrier phase. Depending on the ratio of droplet diameter (D_p) to turbulent length scale l_t [23], the disperse phase is able to consume or generate turbulent kinetic energy in the gas phase flow. This turbulence modulation, i.e., turbulence modification due to the presence of the dispersed phase, is accounted for using the model in [18], as presented in Table 1. For that purpose, the source terms of k and ε (see Table 1) are computed. The constant $c_{\varepsilon,3}^{k-\varepsilon}$ is set 1.87 within this work. It is derived from the experimental data [24]. It depends, however, on the droplet diameter and disperse phase concentration [25]. The determination of the source term for the dissipation of the turbulent kinetic energy was determined by analogy to the dissipation in k-ε turbulence model.

B. Disperse Phase Entrainment

The disperse phase is captured by the Lagrangian approach. Since the density ratio between the disperse phase and the carrier phase is approximately three orders of magnitude greater, the forces considered that contribute to the droplet motion are drag, gravitation and buoyancy forces [24]:

$$\frac{\mathrm{d}u_{p,i}}{\mathrm{d}t} = \frac{3}{4}\frac{C_W}{D_p}\frac{\rho}{\rho_p}|\mathbf{u} - \mathbf{u}_p|(u_i - u_{p,i}) + \frac{(\rho_p - \rho)}{\rho_p}g_i = \frac{1}{m_p}\sum_i F_i \tag{7}$$

The drag coefficient C_W used to model the complex dependencies between the particle and the flow conditions is not constant but depends on relative velocities, viscosities of the disperse phase and carrier phase, the droplet rand shape and the roughness of the particle's surface. The drag coefficient used within this work is determined for a spherical, not deformable, droplet by Eqs. (8) and (9) [24]:

$$C_W = \frac{24}{Re_p}\left(1 + \frac{1}{6}Re_p^{2/3}\right) \qquad Re_p \le 1000 \tag{8}$$

$$C_W = 0.44 \qquad Re_p \ge 1000 \tag{9}$$

where Re_p denotes the particle Reynolds number and is calculated using

$$Re_p = \frac{\rho D_p |u - u_p|}{\mu} \tag{10}$$

To quantify the instantaneous fluid velocity, seen by the droplets in Eq. (7), and its effect on the droplets distribution, the root mean square (RMS) values of the fluid parcel velocity at the droplet location should be modeled. In fact, this is a key question in the disperse phase flow modeling, namely the description of the fluid turbulence along the droplets' trajectories. This can be done using a stochastic Lagrangian process using the fluid turbulent variables. The Markov-sequence model, used within this work, has two main steps in the computation of the fluid element instantaneous fluctuation along the droplet trajectory:

1) The evolution of the fluid element velocity fluctuation along the stream line is determined using the Lagrangian correlation factor.

2) The fluid element velocity fluctuation located at the droplet position is correlated with the fluid element location using the Eulerian correlation factor.

The product of both correlation factors (Lagrangian $R_{L,i}(\Delta t)$ and Eulerian $R_{E,i}(\Delta r)$) yields a new coefficient which can be used to compute the fluctuation of the fluid element $(u_{i,p}'^F)$ at the droplet location [24]

$$R_{p,i}(\Delta t, \Delta r) = R_{L,i}(\Delta t) \cdot R_{E,i}(\Delta r), \quad \text{and} \tag{11}$$

$$u_{i,p}'^F(t_{n+1}) = u_{i,p}'^F(t_n) \cdot R_{p,i}(\Delta t, \Delta r) + \sigma_i \sqrt{1 - R_{p,i}^2(\Delta t, \Delta r)} \cdot \chi_i(t_n) \tag{12}$$

where $\chi_i(t_n)$ denotes a Gaussian random variable, t_{n+1} and t_n are the consecutive time steps. Δr represents the spatial displacements during the time interval Δt.

The turbulent flow in many configurations, however, is not homogenous. Thus, the flow develops stress gradients, which enhance the pressure gradient. Therefore, droplets are shifting to locations of low pressure, i.e., low turbulent intensity. To avoid these phenomena in the Markov-sequence dispersion model, a drift correction term has to be considered, following [26]. The final expressions for the fluid fluctuations at droplet location (fluctuation seen by dispersed phase) are then calculated by

Table 1 Source terms due to the presence of solid particles

ψ	$\bar{S}_{\psi,p,s}$	$\bar{S}_{\psi,p,v}$
1	0	$\sum_p \frac{\dot{m}_{p,v} N_p}{V_{i,j,k}}$
$\bar{u}$	$-\sum_p \frac{\dot{m}_p N_p}{V_{i,j,k}}[(u_p^{t_n+\Delta t} - u_p^{t_n}) - g_x \Delta t]$	$\sum_p \frac{\dot{m}_{p,v} N_p}{V_{i,j,k}} u_p^{t_n}$
$\bar{v}$	$-\sum_p \frac{\dot{m}_p N_p}{V_{i,j,k}}[(v_p^{t_n+\Delta t} - v_p^{t_n}) - g_y \Delta t]$	$\sum_p \frac{\dot{m}_{p,v} N_p}{V_{i,j,k}} v_p^{t_n}$
$\bar{w}$	$-\sum_p \frac{\dot{m}_p N_p}{V_{i,j,k}}[(w_p^{t_n+\Delta t} - w_p^{t_n}) - g_z \Delta t]$	$\sum_p \frac{\dot{m}_{p,v} N_p}{V_{i,j,k}} w_p^{t_n}$
k	$\overline{u_i S_{u_i,p,s}} - \overline{u_i}\,\overline{S_{u_i,p,s}}$	$\overline{u_i S_{u_i,p,v}} - \bar{u}_i \overline{S_{u_i,p,v}} + \frac{1}{2}(\bar{u}_i^2 \overline{S_{\rho,p,v}} - \overline{u_i^2 S_{\rho,p,v}})$
ε	$C_{\varepsilon,3}^{k-\varepsilon}\frac{\varepsilon}{k} S_{k,p,s}$	$C_{\varepsilon,3}^{k-\varepsilon}\frac{\varepsilon}{k} S_{k,p,v}$

$$u_{i,p}^{'F}(t_{n+1}) = u_{i,p}^{'F}(t_n) \cdot R_{p,i}(\Delta t, \Delta r) + \sigma_i \sqrt{1 - R_{p,i}^2(\Delta t, \Delta r)} \cdot \chi_i(t_n) + (1 - R_{p,i}(\Delta t, \Delta r)) T_{L,i} \frac{\partial u_i' u_i'}{\partial x_i} \quad (13)$$

For the Lagrangian correlation factor, an exponential approach was considered:

$$R_{L,i}(\Delta t) = \exp\left(-\frac{\Delta t}{T_{L,i}}\right) \quad (14)$$

where $T_{L,i}$ represents the Lagrangian integral time scale as it is calculated for the k-ε turbulence model, using $T_{L,i} = c_T k/\varepsilon$. When using Reynolds stress models, $T_{L,i}$ is determined (for all direction, x, y and z) by

$$T_{L,i} = c_T \frac{\sigma_i^2}{\varepsilon} \quad (15)$$

where the constant c_T equals 0.3 and σ_i^2 denotes $\overline{u_i' u_i'}$. The Eulerian correlation factor $R_{E,i}(\Delta r)$ is computed using longitudinal and transversal correlation functions $f(\Delta r)$ and $g(\Delta r)$as follows:

$$R_{E,i}(\Delta r) = (f(\Delta r) - g(\Delta r)) \frac{\Delta r_i \Delta r_j}{\Delta r^2} + g(\Delta r)\delta_{ij} \quad (16)$$

.

The longitudinal and transversal correlation functions $f(\Delta r)$ and $g(\Delta r)$ are computed using the following expressions:

$$f(\Delta r) = \exp\left(-\frac{\Delta r}{L_E}\right); \qquad g(\Delta r) = \left(1 - \frac{\Delta r}{2L_E}\right) \exp\left(-\frac{\Delta r}{L_E}\right) \quad (17)$$

where L_E represents a simplified turbulent length scale, which is determined by

$$L_E = c_L T_L \sigma \quad (18)$$

T_L is computed according to Eq. (15) and c_L represents a model constant set to 3.0, as given in [26].

C. Evaporation Model

The uniform temperature model by Abramzon and Sirignano [19] and Sirignano [27] was applied to evaporation. The model describes the evolution of the droplet's temperature and diameter, i.e., evaporation rate and energy flux through the liquid/gas interface. This model is based on the film thickness theory. It does not consider any temperature variation in the interior of the droplets (homogenous temperature). However, the temperature variation has an unsteady nature and is accompanied by an unsteady mass transition. As this model does not account for the gradient at the interior of the droplet, the latter ones are not discretized. Therefore, this model does not require long computing times. The following basic assumptions and simplifications were made to reduce the complexity of the theoretical description:

1) Droplets are assumed spherical.

2) Secondary atomization and coalescence of droplets are neglected, i.e., simple elastic collisions between droplets and wall are assumed without any kind of film formation.

3) The influence of the surface tension is neglected, i.e., uniform pressure around the droplet is assumed.

4) Uniform physical properties of the surrounding fluid and liquid-vapor thermal equilibrium on the droplet surface are assumed.

5) The ambient air is not soluble in the droplet fluid.

6) Chemical reactions and radiation are not considered.

7) One component model is considered (the infinite conductivity model).

The vaporization rate $\dot{m}_{p,v}$ is calculated by considering the mass transfer around the droplet, following [28,29]:

$$\dot{m}_{p,v} = 2\pi r_p \overline{\rho_m D_m} Sh^* \ln(1 + B_M) \quad (19)$$

where r_p is the droplet radius, and $\bar{\rho}_m$ and $\bar{D}_m$ are the averaged values of the mixture density and binary diffusion coefficient throughout the film, respectively. B_M represents Spalding's mass transfer number, defined by

$$B_M = \frac{y_s - y_\infty}{1 - y_s} \quad (20)$$

in which y_s is the surface vapor mass fraction and y_∞ is the vapor mass fraction far from the droplet. In particular, y_s depends on the vapor relative pressure, which itself depends on the droplet surface temperature:

$$y_s = \frac{\upsilon_{s,\mathrm{eq}}}{\upsilon_{s,\mathrm{eq}} + (1 - \upsilon_{s,\mathrm{eq}})\theta_2} \quad (21)$$

where θ_2 is the ratio of molecular weights. The equilibrium molar mass fraction $\upsilon_{s,\mathrm{eq}}$ is related to the saturation pressure through the Clausius–Clapeyron equation. The accuracy of the evaporation rate depends strongly on determining the values of $\bar{\rho}_m$ and $\bar{D}_m$. Physical properties of the air vapor mixture (in the gaseous film around the droplet) are determined using the reference temperature and mass fraction. They are calculated using the Simpson or Sparrow and Gregg 1/3 rule, see Berlemont et al. [29], from which the best estimate of these quantities was obtained. The droplet radius is obtained from the equation of the diameter evolution for each droplet by

$$\frac{\mathrm{d}D_p}{\mathrm{d}t} = -\frac{2\dot{m}_{p,v}}{\pi \rho_L D_p^2} - \frac{D_p}{3\rho_L} \frac{\partial \rho_L}{\partial T_p} \frac{\mathrm{d}T_p}{\mathrm{d}t} \quad (22)$$

where ρ_L is the liquid density, and T_p the droplet temperature. Effects of convection on the vaporization and the heat flux rate are taken into account using semi-empirical correlations, such as those for the Sherwood number and the Nusselt number.

The quantity Sh^* in Eq. (19) denotes the modified Sherwood number, which includes the effects of the Stefan flow. It is defined by

$$Sh^* = 2 + \frac{Sh_0 - 2}{F_M} \quad (23)$$

where Sh_0 (24) represents the Sherwood number in negligible evaporation, i.e., the Stefan flow is not accounted for:

$$Sh_0 = 1 + (1 + Re_p Sc_p)^{1/3} f(Re_p) \quad (24)$$

where Sc_p is the Schmidt number, while $f(Re)$ is an empirical function defined as

$$f(Re_p) = Re_p^{0.077} \quad (25)$$

The function F_M in Eq. (23) represents a correction factor, which takes into consideration the relative change in the mass film thickness due to the droplet evaporation process [30]:

$$F_M = F_M(B_M) = (1 + B_M)^{0.7} \ln \frac{(1 + B_M)}{B_M} \quad (26)$$

The evaporation is coupled with the droplet energy/heating in (22) where the droplet temperature variation is described by

$$\frac{\mathrm{d}T_p}{\mathrm{d}t} = -\frac{6\dot{Q}_1}{\rho \pi c_{pL} D_p^3} \quad (27)$$

where c_{pL} denotes the heat capacity coefficient of the liquid and $\dot{Q}_L$ the heat flux rate penetrating into the droplet is determined by

$$\dot{Q}_l = \dot{m}_{p,v}\left(\frac{c_{pm}(T_\infty - T_p)}{B_T} - h_v(T_p)\right) \quad (28)$$

In Eq. (28), $h_v(T_P)$ expresses the effective latent heat of vaporization. It is a function of temperature and varies with the liquid used. B_T is the Spalding heat transfer number expressed by

$$B_T = \frac{\bar{c}_{p,v}(T_\infty - T_P)}{r(T_p) + \dot{Q}_l/\dot{m}_{p,v}} \tag{29}$$

and is related to the mass transfer number B_M by

$$B_T = (1 + B_M)^\phi - 1 \tag{30}$$

where

$$\phi = \frac{c_{p,v}}{c_{p,m}} \frac{Sh^*}{Nu^*} \frac{1}{\overline{Le}} \tag{31}$$

The variable ϕ depends on the thermophysical properties, the Lewis number Le, and the modified Sherwood and Nusselt numbers (Sh^* and Nu^*). The modified Nusselt number in (31) is defined by

$$Nu^* = 2 + \frac{Nu_0 - 2}{F_T} \tag{32}$$

where

$$Nu_0 = 1(1 + Re_p Pr)^{1/3} f(Re_p) \tag{33}$$

expresses the Nusselt number for a spherical droplet with negligible evaporation, while the function $f(Re_p)$ is computed using Eq. (25). F_T is a correction factor for the change in temperature that occurs within the film thickness due to the droplet evaporation process [30]:

$$F_T = F_T(B_T) = (1 + B_T)^{0,7} \ell_n \frac{(1 + B_T)}{B_T} \tag{34}$$

In (31), c_{pv} and c_{pm} are the heat capacity coefficients of vapor and mixture, respectively. There was no correction to the drag coefficient due to the evaporation process. The gas viscosity in the droplet Reynolds number near the droplet was estimated at a well-defined reference state of temperature and vapor mass fraction according to the averaging 1/3 rule.

D. Coupling Between the Eulerian and Lagrangian Codes

The interaction between the continuous and dispersed phases is demonstrated using the coupling between the two codes. Following a steady method after the convergence of gas phase, the gas variables are kept frozen and all the droplets representing the entire spray are injected into the computational domain. Because of the presence of the droplets source terms, the conventional residuals are characterized by a jump after each coupling. To avoid the resulting fluctuations, an additional underrelaxation technique should also be employed for droplet source terms. The algorithm alternates repeatedly between these two steps until convergence is reached. The issue of convergence of the Eulerian–Lagrangian coupling has been debated in many papers, for example in [31]. The criteria that depend on the specifics of the problem may change during the evolution of a problem. Unfortunately, there are no universal guidelines for selecting criteria because they depend not only on the physical processes being approximated but also on the details of the numerical formulation. For example, the normalized residual method is used for single-phase flow but not for multiphase flows. The principal reason is the stochastic nature of the Lagrangian procedure and the associated source term fluctuations within every coupling between the phases. These fluctuations, as mentioned above, depend strongly on the spatial smoothness of droplet source term distributions.

In the frame of this work, convergence of the Eulerian–Lagrangian coupling procedure is reached when the fluid's properties do not

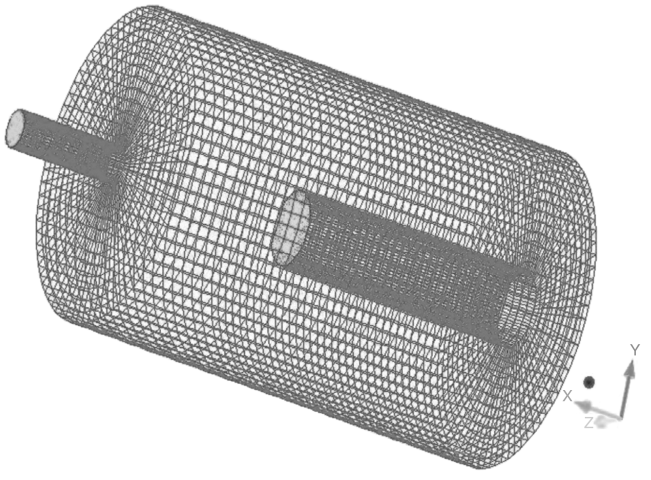

Fig. 10 Numerical grid used representing the pressure chamber.

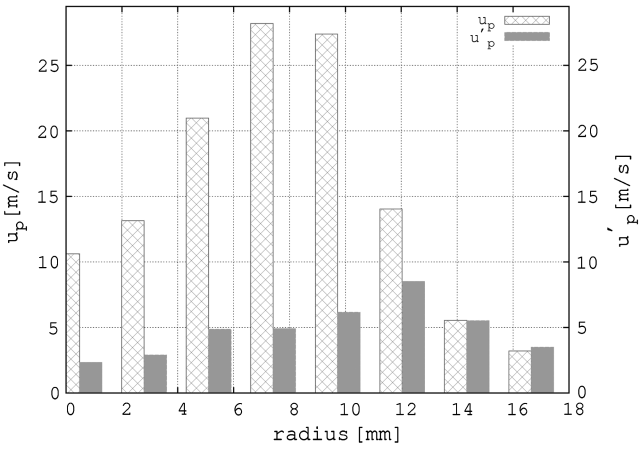

Fig. 11 Droplet axial inlet velocity and fluctuations for the test case 1 bar.

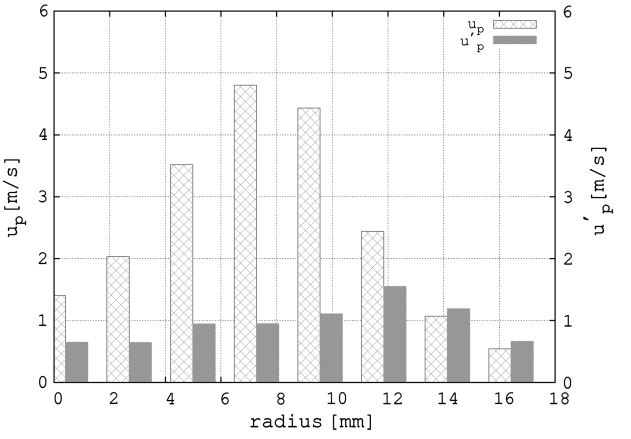

Fig. 12 Droplet axial inlet velocity and fluctuations for the test case 5 bar.

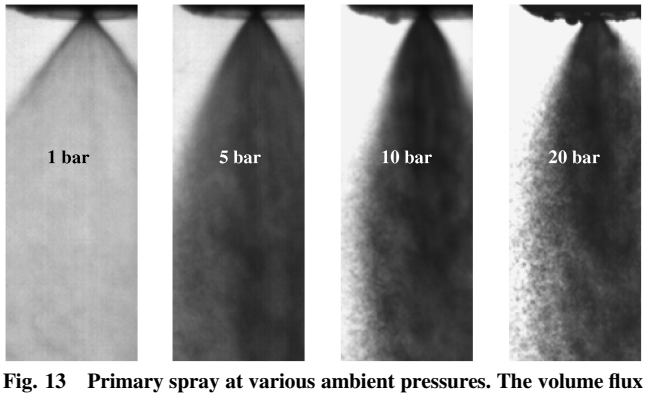

Fig. 13 Primary spray at various ambient pressures. The volume flux of the liquid is constant.

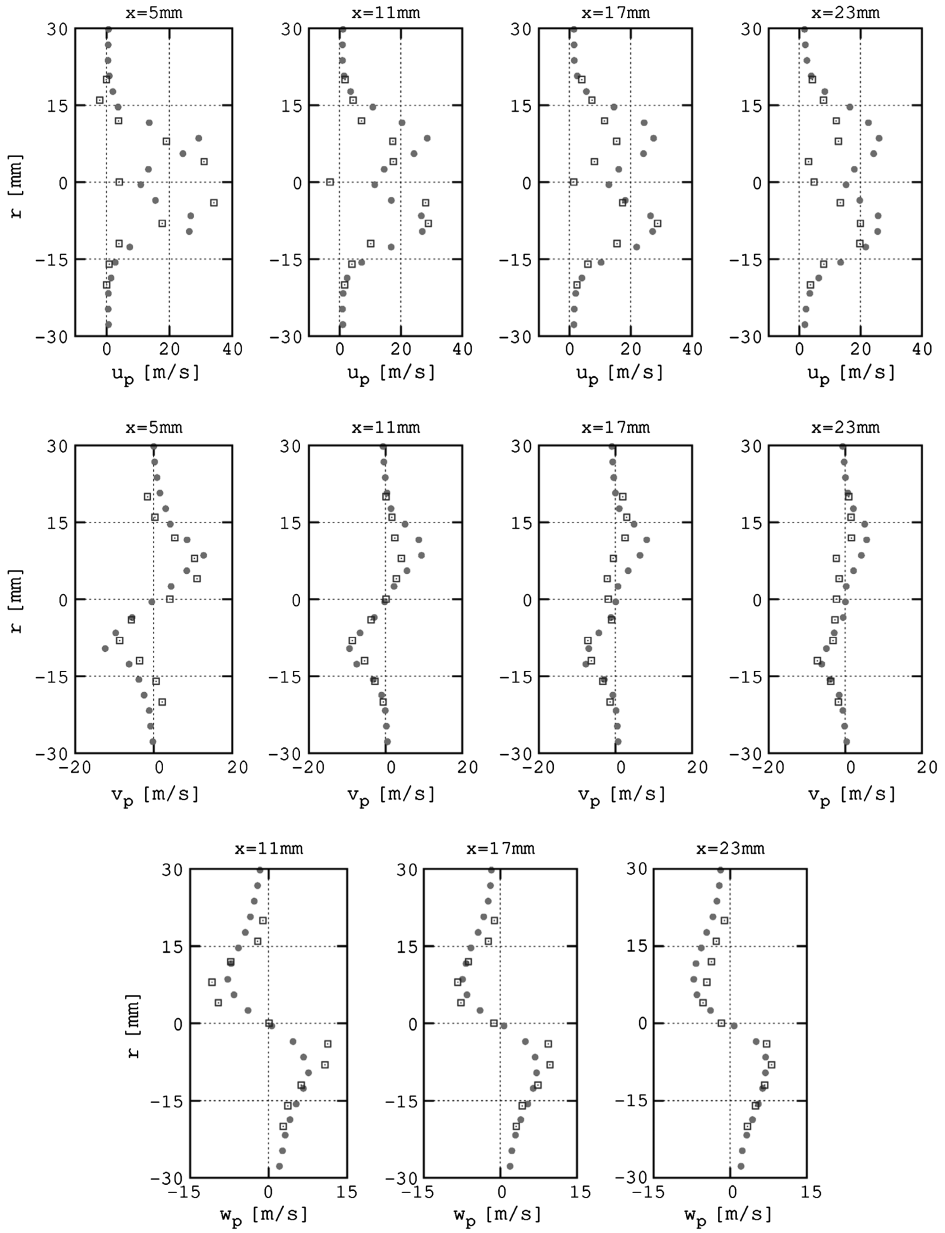

Fig. 14 Droplet mean velocity components (axial, radial and azimuthal): comparison between the numerical prediction (● ● ●) and experimental data (□ □ □) at the ambient pressure of 1 bar.

change their value from one coupling to the next in the presence of droplets. Convergence of the Eulerian–Lagrangian coupling is sensitive to the total number of numerical droplets considered. The carrier phase volume variation caused by water droplets is neglected. This assumption is acceptable [32], since the droplet volume fraction, $\alpha_p = \sum_{i=1}^{n} V_{p,i}/V_{i,j,k}$, that describes the amount of disperse phase volume within the gas phase is about 0.3×10^{-4}. The parameter $V_{p,i}$ denotes the volume of particle i within the considered control volume$V_{i,j,k}$.

Typical droplet volume fraction for practical gas turbine conditions in aircraft engines is approximately equal to 1.53×10^{-4} (e.g. Rolls Royce combustor BR710) [33].

For accurate statistics, a sufficiently large number of water droplets were dispersed in air. However, there is no one-to-one correlation between real and numerical droplets to reduce computational time [34]. Thus, individual droplet paths are tracked through the flowfield, based on a force balance on each entity [31], solving the equations of motion using Euler's forward integration method [35]. This method is numerically efficient but depends strongly on the prescribed gas phase velocity field. The path lines of one droplet may coincide with the streamline of the continuous phase field, particularly when evaporating droplets reach the diameter close to that of the seeding particles. In some cases the streamline features a closed profile, e.g., in the recirculation zone, so the droplets follow the streamline and do not leave the computational domain. This occurs mainly with solid particles because they do not disappear due to evaporation, so that coupling between the Lagrangian and Eulerian codes could not be achieved before all particles leave the configuration due to the steady nature of the coupling. If droplets enter a recirculation zone or a region with zero velocity gradients, they remain located there and do not leave the computational domain. Therefore, additional stopping conditions were added (the number of iterations should be smaller than 10,000 time steps) to avoid formation of spirals.

E. Boundaries Conditions and Numerical Setup

The inlet boundary conditions for the combustion chamber corresponded to scaled gas turbine conditions. From experimental results at different pressures, the cases with $P_{\text{inl}} = 1$ bar and $P_{\text{inl}} = 5$ bar were simulated. The mass flow rate boundary condition for the gas phase equals 20 m^3/h. The swirler was not included in the

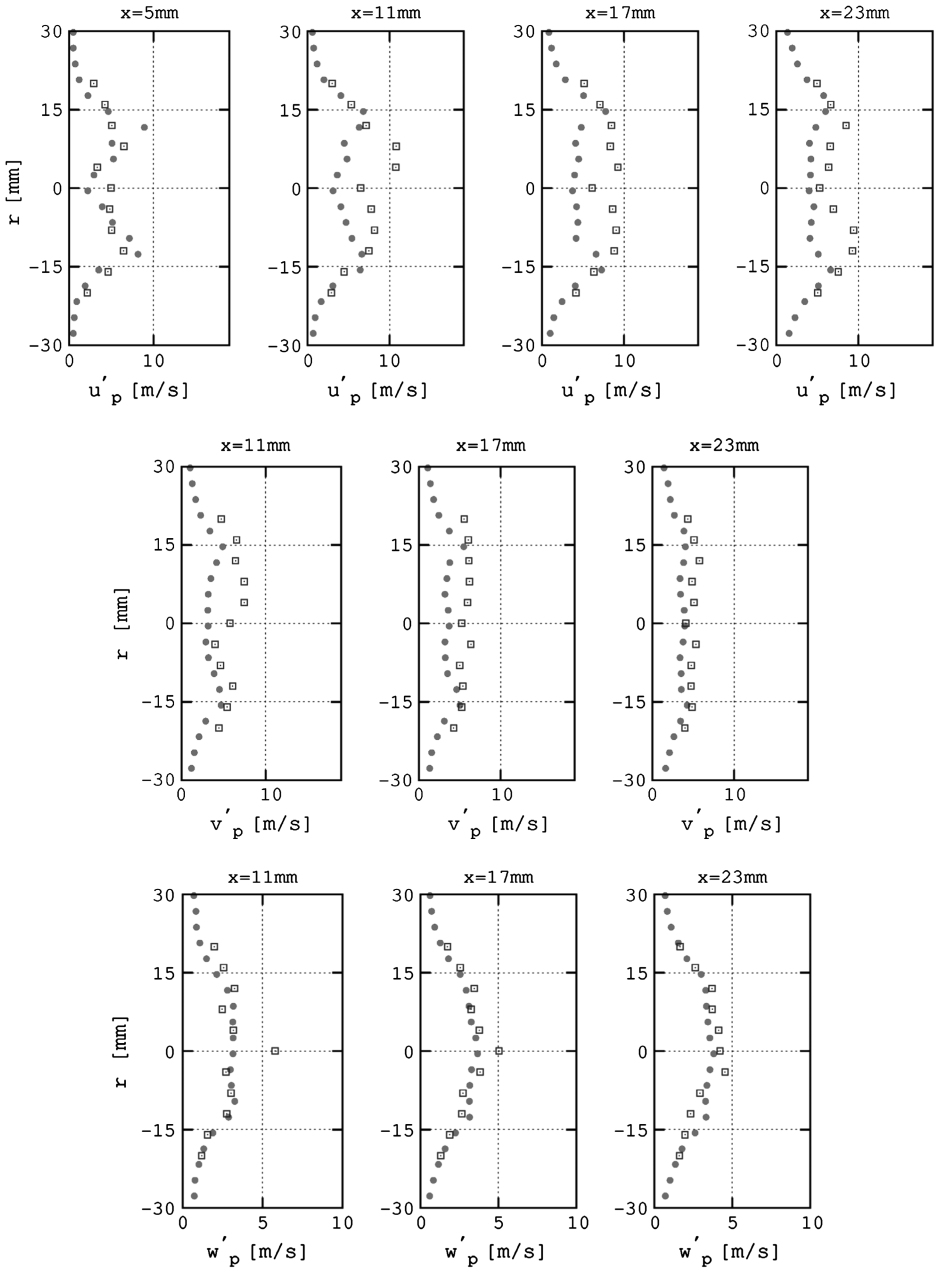

Fig. 15 Droplet velocity RMS: comparison between the numerical prediction (● ● ●) and experimental data (□ □ □) at the ambient pressure of 1 bar.

computational domain. Nevertheless, appropriate boundary conditions at the inlets were imposed by the velocity profiles, as shown by measurements for the single-phase flow. The boundary condition for the turbulent kinetic energy corresponded to a turbulence intensity of 25% of the resultant velocity through the inlet. It agreed with the measured RMS profile of axial, radial and tangential velocities, using the definition $0.5(u'^2 + v'^2 + w'^2)$. The dissipation rate was estimated using expression (35). The turbulent length scale was assumed to be equal to the diameter of the hole or inlet opening:

$$\varepsilon = C_\mu^{3/4} \frac{k^{3/2}}{0.41 \cdot \Delta r} \tag{35}$$

where $C_\mu = 0.09$ and Δr is the width of the annulus.

The mesh for the configuration (Fig. 10) includes 18 multi-connected domains, that is, they consist of several separate flow-paths that interact with each other. Hexahedral cells were used to generate the mesh.

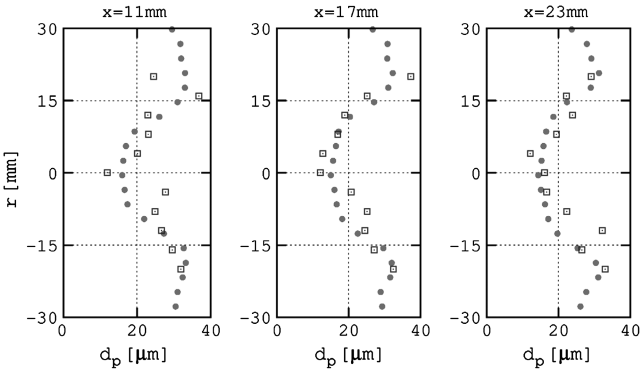

Fig. 16 Average spray droplet diameter as a function of the transverse coordinate: comparison between the numerical prediction (● ● ●) and experimental data (□ □ □) at the ambient pressure of 1 bar.

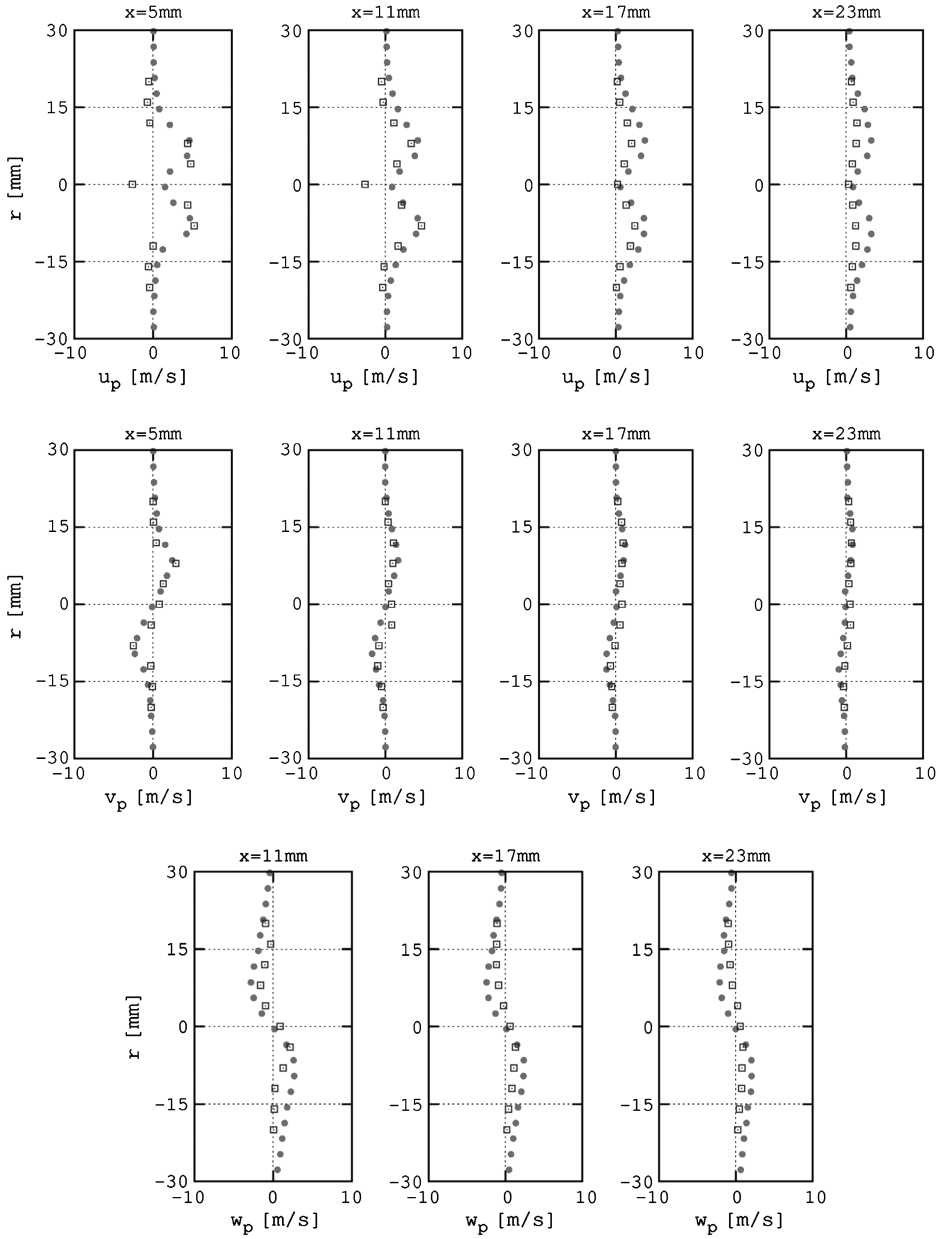

Fig. 17 Droplet mean velocity components (axial, radial and azimuthal): comparison between the numerical prediction (● ● ●) and experimental data (□ □ □) at the ambient pressure of 5 bar.

The disperse phase was injected with the mass flow rate of 0.7 kg/h. The boundary conditions for the disperse phase were defined according to the experimental data.

The flowfield in the chamber is influenced remarkably by the variation of the ambient pressure which is also a measure of the backpressure. Since the mass flow rate of the carrier phase was kept constant, the inlet velocity has changed reciprocally to the pressure augmentation. Water droplets exhibited relatively small diameters revealing a mean stokes number close to the unity. These droplets are likely to follow the carrier phase, therefore the numerical boundary conditions for the inlet velocity components were affected by the variation of the ambient pressure which engender varying backpressure. Figures 11 and 12 show the axial droplet velocity with the corresponding fluctuations for 1 and 5 bar, respectively. Kenny et al. [36] studied the effect of chamber backpressure on fluid mechanics of the swirl injector. They realized that the spray angle has decreased while increasing the backpressure. This remark is also confirmed in the current investigation. Figure 13 shows the decrease of the spray opening angle for augmenting ambient pressure. The poly disperse spray includes eight classes that distinguish on the diameters, mass flow rate, velocities, fluctuations and injection locations. For the generation of statistically reliable results a total number of 160,000 parcels trajectories were tracked each coupling between both phases. The increase in parcel number has no influence on the droplet properties, thus ensuring statistical independence.

IV. Comparison Between the Simulation and the Experiment

The prediction of droplet properties under turbulent conditions is strongly related to the description of the gas phase turbulent flow and the associated complex interaction with the dispersed phase. Therefore, the simulations of the gas phase were performed first. A comparison of the streamlines, the isotherms and the cross-sectional profiles of axial, gas phase velocity with experimental data shows qualitatively plausible agreement between experiment and simulation (not shown). The results presented were obtained using the standard $k-\varepsilon$ model in which the source term for the two-way coupling was included, as described previously. In Figs. 14 and 15, droplets mean velocity components and their RMS as a function of the transverse coordinate are shown for the ambient pressure of 1 bar. In Fig. 16, the radial distribution of the mean spray diameter as a

function of the transverse coordinate is displayed, comparing the numerical prediction with experimental data. The asymmetry seen in the axial velocity profile for $x \geq 11$ mm may be caused by errors in the nozzle mounting and pipe installations as mentioned in Secs. III.B and III.C. Instabilities or resonance problems that impact the atomization and form clusters are not excluded.

Some disagreements in velocity components at the centerline of the configuration were observed. Numerically, the droplets are not able to capture the negative axial velocity (up) 11 mm downstream of the nozzle exit, however, the maximum values agree favorably with the experimental data. The discrepancy is mainly observed in the recirculation zone where droplets display their smallest average diameter; ca. 18 μm. Being small, the droplets are not able to impose their own motion dynamics but follow up the stream lines of the carrier phase which, due to the high swirl number, has a large recirculation zone in the centerline of the configuration demonstrating an important negative axial velocity that was not well captured numerically by the Reynolds-averaged Navier–Stokes (RANS) turbulence model. The predicted radial (vp) and tangential (wp) droplet velocity components show good agreement with the experimental data. Because of the centrifugal forces, the radial droplet velocity is up to 15 m/s. It is worth noting that the drift factor, used in the dispersion model to determine the fluid element instantaneous velocity, plays an important effect in the disperse phase entrainment. The tangential velocity has a similar profile, featuring high velocity up until the cross section 23 mm downstream, while the radial component decreases rapidly and displays negligible values at the last cross section. This could be because of the different momentum transfer from the axial to the radial and tangential directions.

The droplet axial velocity fluctuation demonstrates deviations in the cross sections at 11, 17 and 23 mm. The profiles show two relative maximums located at the edges of the spray jets. High shear flow phenomena dominate the two-phase flow in these locations. The discrepancy might originate from the disagreement observed at the droplet mean axial velocity. Indeed, an underprediction of the axial profiles reveals an underestimation of the droplet RMS values. The droplet radial and tangential velocity fluctuations show good agreement founded upon the accurate prediction of the mean velocities, vp and wp.

Worth noting is that the radial velocity fluctuation at 11 mm downstream feature a value that is larger than its mean. The reasons

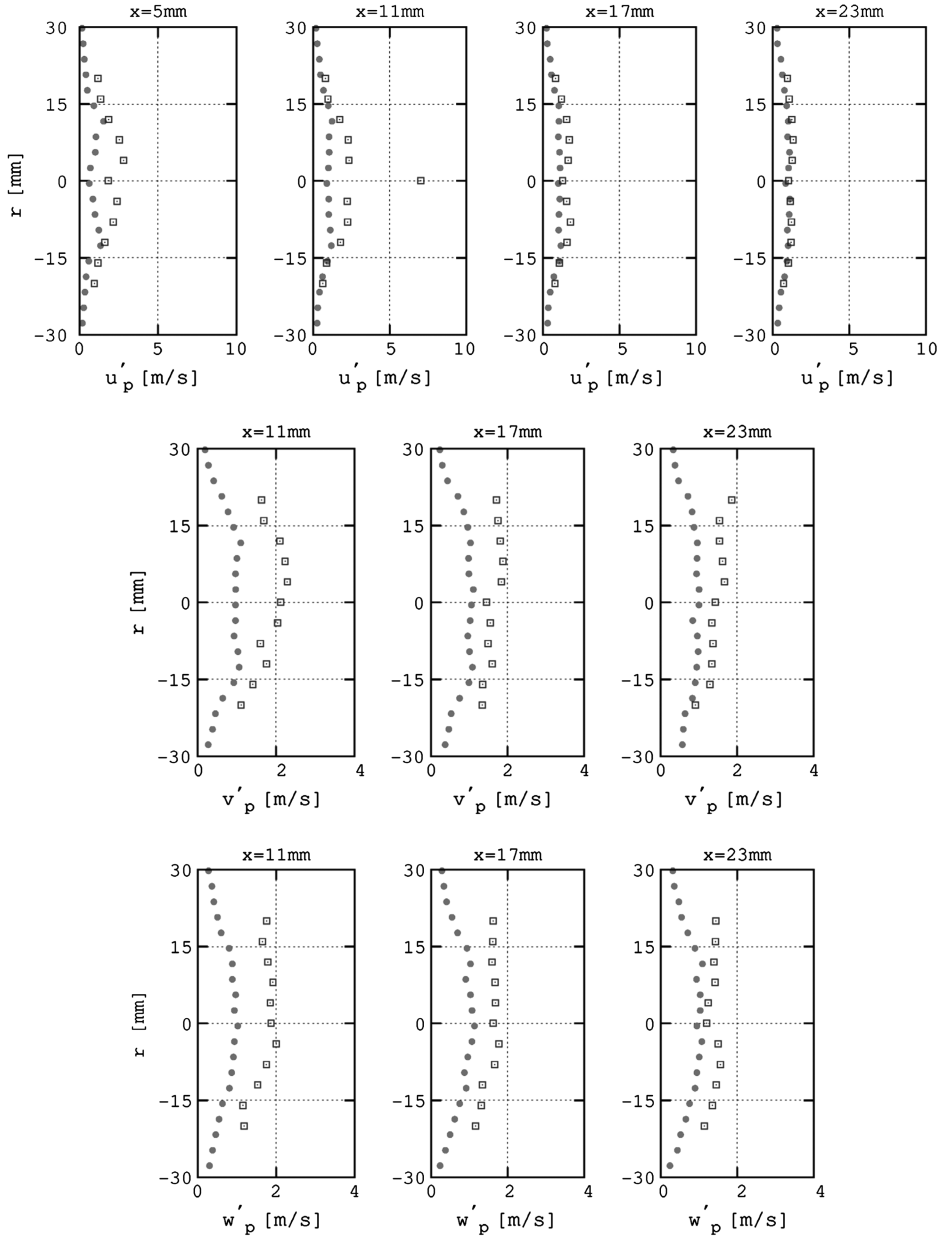

Fig. 18 Droplet velocity RMS: comparison between the numerical prediction (● ● ●) and experimental data (□ □ □) at the ambient pressure of 5 bar.

behind this appearance could be the formation of high velocity gradients. Since the radial velocity is mainly generated due to the sudden expansion in the geometry which is seen by the flow at nozzle exit, this effect is rapidly decreased while moving downstream. Thus the mean value of the radial velocity reduces remarkably, which in turn increase the velocity gradients that represents the production terms for higher fluctuations.

The distribution of the droplet mean diameter reveals plausible agreement between the experimental and numerical results. The temperature of the carrier phase at 1 bar equals the environmental condition, i.e., 24°C, thus no significant effect of the phase transition was observed. Indeed, the profile is adequately captured numerically and the evaporation model predicts the phase transition under environment conditions well. The minimum mean droplet diameter at the centerline equals ca. 12 μm whereas the maximum aimed for is 38 μm, demonstrating an important range of droplet classes that differ in diameter and velocity components, velocity fluctuations, injection location and mass flow rate. Droplets with large diameters are located around the radial position $r = 15$ mm, forming the spray jet and featuring high axial velocities.

The same properties are found at an ambient pressure of 5 bar (Figs. 17–19). The agreement at 5 bar is more satisfactory for the droplet velocity components, except at positions $x = 5$ and 11 mm because of a deficiency in exactly capturing the recirculation zone of the carrier phase using the RANS approach, despite the use of turbulence modulation models which respect generation or dissipation of turbulence caused by the presence of the dispersed phase. The predicted axial velocity fluctuations at the pressure of 5 bar show good agreements with the experimental data, whereas the radial and tangential ones are underpredicted, however, the quantitative underestimation did not exceed 1 m/s. A high turbulence level was measured for the water droplets, which provide important values for the velocity RMS (Fig. 18). The recorded droplet velocity fluctuations display notably unchanged profiles for the radial and tangential direction, having an order of magnitude of more than 50% of their mean values.

Since the mass flow rate of the carrier phase was kept constant during measurement at all pressures, a reduction of the mean velocity component by 5 bar was observed (compared with the test case reduction of 1 bar) due to the augmentation of the gas density. The two-phase flow remains, however, highly turbulent. The droplets at the centerline have small diameters of less than 20 μm, contributing to Stokes number close to the unity. Consequently, they seek the path of tracer particles and flow along the gas phase streamlines.

The unexpectedly high level of droplet turbulence intensity at 5 bar is not easily interpreted. The disperse phase has reduced the mean velocity while increasing the pressure (due to the slowed carrier phase) but the RMS remain at the same level. One possible reason for these elevated RMS may be the assigned injection positions of the droplets; they are inserted with a particular opening angle and are distributed around the edge of the recirculation zone. Thus the droplets are subjected to an important shear flow phenomenon of the gas phase with high mean velocity gradients, which are responsible for the enhanced production of turbulence.

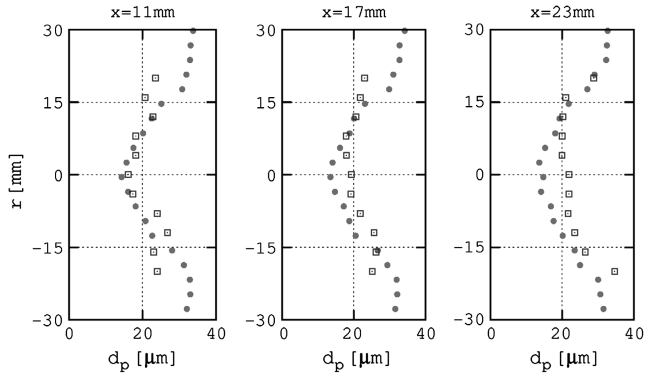

Fig. 19 Average spray droplet diameter as a function of the transverse coordinate: comparison between the numerical prediction (● ● ●) and experimental data (□ □ □) at the ambient pressure of 5 bar.

The discrepancies between the numerical and experimental results could be caused by the two-phase flow not being stationary. Recent spray visualization and statistical analysis of the phase Doppler data show that both the disperse (liquid) and continuous (gas) phases oscillate [37]. The frequency of these oscillations reduces at higher ambient pressures whereas the amplitude of the fluctuations of the spray density significantly increases as the ambient pressure becomes higher. The unsteady effect associated with these oscillations has not been accounted for in the code at this stage in steady calculations. The profiles of the droplet diameter display some differences between the numerical and experimental data at the cross section 17 mm downstream. An augmentation of the mean diameter is detected experimentally while spreading further downstream at the radial position $|r| \geq 15$ mm. This physical behavior justifies droplet coalescence, a phenomenon not accounted for numerically. The evaporation does not manifest remarkably, since the temperature of the surrounding gas was close to environmental conditions. Augmentation of the pressure suppresses the phase transition processes. Despite the many complex interacting physical phenomena, the overall agreement points to the accuracy of the evaluation techniques used for measuring. Numerical simulations yield results for both back pressures that exhibit an overall satisfactory agreement with experiments. It should be stressed that it was very difficult to collect the experimental data exactly in the vicinity of the droplet injection nozzle due to the instrument configuration and the presence of high loading of droplets, along with atomization processes that are not yet included in the numerical spray model used for predictions reported in this work.

V. Conclusions

An experimental and numerical study of the effect of high-pressure conditions on spray generation was performed, permitting an understanding of important aspects of the droplets produced by an airblast atomizer. The experiments showed that the chamber pressure has a strong effect on the droplet diameters; when increasing the chamber pressure, the droplet diameters grow accordingly. Increasing the chamber pressure from 1 to 5 bar did not affect the droplet evaporation remarkably at atmospheric temperature conditions. The uniform temperature evaporation model predicted the experimental data well for one component substance. At 5 bar, an unexpectedly high level of droplet turbulence intensity was recorded. This could be attributed to the important shear flow that the spray was subjected to within the recirculation zone. Enhancing the pressure inside the chamber produced remarkable variations in the axial droplet velocity profile. An obvious drop in the disperse phase speed, which was related to the slowing of the carrier phase, was attributed to the interaction between both flows inside the airblast atomizer.

The models used for droplet dispersion, tracking and coupling between the two phases showed good agreement overall. Therefore this approach can be used as a base for further model improvement. Higher turbulence models, e.g. large eddy simulation, should be adopted for the gas phase for better prediction of the spray characteristics. Moreover, the two-way coupling should be extended to four ways where droplet coalescence and collision are considered. The spray breakup is a challenging issue that should be modeled and taken into account.

It is important to focus further investigations on the source of droplet injection and detect the properties of the disperse and gas phases inside the swirler, so that the effect of high pressure can be better examined. Besides the augmentation of the inside chamber pressure, it is important to investigate the droplet behavior under a simultaneous increase in pressure and carrier phase temperature.

Acknowledgments

The authors acknowledge financial support from the Deutsche Akademischer Austausch Dienst and the financial support of

Deutsche Forschungsgemeinschaft through grant 52100658 in the framework of Sonder Forschungsbereich 568.

References

[1] Lefebvre, A. H., *Gas Turbine Combustion*, Hemisphere, Washington, D.C., 1983.

[2] Lefebvre, A. H., *Atomization and Sprays*, Hemisphere, New York, 1989.

[3] Liu, H., *Science and Engineering of Droplets: Fundamentals and Applications*, Noyes, New York, 1981.

[4] Biswas, M. N., "Atomization in Two-Phase Critical Flows," *Proceedings of the Second International Conference on Liquid Atomization and Sprays*, 1982, pp. 145–151.

[5] Dobre, M., and Bolle L., "Practical Design of Ultrasonic Spray Devices: Experimental Testing of Several Atomizer Geometries," *Experimental Thermal and Fluid Science*, Vol. 26, Nos. 2–4, June 2002, pp. 205–211. doi:10.1016/S0894-1777(02)00128-0

[6] Ingebo, R. D., "Effect of Mass-Velocity on Liquid Jet Atomization in Mach 1 Gas Flow," *Proceedings of the Fourth International Conference on Liquid Atomization and Spray Systems*, Japan, 1988.

[7] Becker, J., and Hassa, C., "Breakup and Atomization of a Kerosene Jet in Cross Flow of Air at Elevated Pressure," *Proceedings of ILASS-Europe'99*, Toulouse, France, 1999.

[8] Becker, J., and Hassa, C., "Experimental Investigation of Spatial and Temporal Aspects of the Liquid Fuel Placement in a Swirl Cup at Elevated Pressure," *Proceedings of ASME Turbo Expo*, GT2004-53524, 2004.

[9] Becker, J., Heitz, D., and Hassa, C., "Spray Dispersion in a Counter-Swirling Double-Annular Airflow at Gas Turbine Conditions," *Proceedings of ILASS-Europe*, Zurich, 2001.

[10] Sadiki, A., Chrigui, M., Janicka, J., and Maneshkarimi, M., "Modelling and Simulation of Effects of Turbulence on Vaporization Mixing and Combustion of Liquid-Fuel Sprays," *Flow, Turbulence and Combustion*, Vol. 75, Nos. 1–4, 2005, pp. 105–130. doi:10.1007/s10494-005-8579-0

[11] Krebs, W., Gruschka, U., Fielenbach, C., and Hoffmann, S., "CFD Analysis of Reacting Flow in an Annular Combustor," *Progress in Computational Fluid Dynamics*, Vol. 1, Nos. 1–3, 2001, pp. 104–116. doi:10.1504/PCFD.2001.001475

[12] Sankaran, V., and Menon, S., "LES of Spray Combustion in Compressible High Reynolds Number Swirling Flows," *Proceedings of the Second International Symposium on Turbulence and Shear Flow Phenomena*, 2001.

[13] Sornek, R. J., Dobashi, R., and Hirano, T., "Effect of Turbulence on Vaporization, Mixing, and Combustion of Liquid-Fuel Sprays," *Combustion and Flame*, Vol. 120, No. 4, 2000, pp. 479–491. doi:10.1016/S0010-2180(99)00105-4

[14] Gäokalp, I., Chauveau, C., Simon, O., and Chesneau, X., "Mass Transfer from Liquid Fuel Droplets in Turbulent Flow," *Combustion and Flame*, Vol. 89, Nos. 3–4, 1992, pp. 286–298. doi:10.1016/0010-2180(92)90016-I

[15] Chrigui, M., Ahmadi, G., and Sadiki, A., "Study on Interaction in Spray Between Evaporating Droplets and Turbulence Using Second Order Turbulence RANS Models and a Lagrangian Approach," *Progress in Computational Fluid Dynamics*, Vol. 4, Nos. 3–5, 2004, pp. 162–174. doi:10.1504/PCFD.2004.004084

[16] Zhu, G., and Aggarwal, S., "Transient Supercritical Droplet Evaporation with Emphasis on the Effects of Equation of State," *International Journal of Heat and Mass Transfer*, Vol. 43, No. 7, 2000, pp. 1157–1171. doi:10.1016/S0017-9310(99)00197-0

[17] Klose, G., Schmehl, R., Meier, R., Meier, G., Koch., R., and Wittig, S., "Evaluation of Advanced Two-Phase Flow and Combustion Models for Predicting Low Emission Combustors," *Proceedings of ASME Turbo Expo*, Munich, 2000.

[18] Chrigui, M., Hage, M., Sadiki, A., Janicka, J., and Dreizler, A., "Experimental and Numerical Analysis of Spray Dispersion and Evaporation in a Combustion Chamber," *Atomization and Sprays*, Vol. 19, No. 10, 2009, pp. 929–955. doi:10.1615/AtomizSpr.v19.i10.30

[19] Abramzon, B., and Sirignano, W. A., "Droplet Vaporization Model for Spray Combustion Calculations," *International Journal of Heat and Mass Transfer*, Vol. 32, No. 9, 1989, pp. 1605–1618. doi:10.1016/0017-9310(89)90043-4

[20] Olson, E. O., "Fuel Nozzles for Oil Burners, Technical Aspects of Applications," Delavan Fuel Meeting Products Operation, Bamberg, South Carolina, www.delavaninc.com/pdf/Fuel_Nozzles_for_Burners.PDF.

[21] Batarseh, F. Z., Roisman, I. V., and Tropea, C., "Spray Generated by an Airblast Atomizer at High-Pressure Conditions," *Proceedings of ASME Turbo Expo*, Montreal, GT2007-27803, March 2007.

[22] Crowe, C. T., *Multiphase Flow Handbook*, Sec. 12, 2005, p. 116.

[23] Gore, R. A., and Crowe, C. T., "Effect of Particle Size on Turbulent Intensity," *International Journal of Multiphase Flow*, Vol. 15, No. 2, 1989, pp. 279–285. doi:10.1016/0301-9322(89)90076-1

[24] Sommerfeld, M., "Modellierung und numerische Berechnung von partiklebeladenen turbulenten Strömungen mit Hilfe des Euler/Lagrange-Verfahrens," Shaker Verlag, Aachen, Germany, 1996.

[25] Squires, K. D., and Eaton, J. K., "On the Modeling of Particle-Laden Turbulent Flows," *Proceedings of the Sixth Workshop on Two-Phase Predictions*, Vol. 14, 1993, pp. 220–229.

[26] Sommerfeld, M., Kohnen, G., and Rüger, M., "Some Open Questions and Inconsistencies of Lagrangian Particle Dispersion Models," *Proceedings of the Ninth Symposium on Turbulent Shear Flow*, Tokyo, Paper 5.1, 1993.

[27] Sirignano, W. A., "Fluid Dynamics of Sprays," *Journal of Fluids Engineering*, Vol. 115, No. 3, 1993, pp. 345–378. doi:10.1115/1.2910148

[28] Park, J. H., Yoon, Y., and Hwang, S. S., "Improved Tab-Model for Prediction of Spray Droplet Deformation and Breakup, Atomization and Sprays," Vol. 12, No. 4, 2002, pp. 387–402. doi:10.1615/AtomizSpr.v12.i4.20

[29] Berlemont, A., Grancher, M. S., and Gouesbet, G., "Heat and Mass Transfer Coupling Between Vaporizing Droplets and Turbulence Using a Lagrangian Approach," *International Journal of Heat and Mass Transfer*, Vol. 38, No. 16, 1995, pp. 3023–3034. doi:10.1016/0017-9310(95)00025-5

[30] Abramzon, B., and Sirignano, W. A., "Approximate Theory of a Single Droplet Vaporization in a Convective Field: Effects of Variable Properties, Stefan Flow and Transient Liquid Heating," *Proceedings of the 1987 ASME/JSME Thermal Engineering Joint Conference*, Honolulu, Vol. 1, 22–27 March 1987, pp. 11–18.

[31] Kohnen, G., Rüger, M., and Sommerfeld, M., "Convergence Behavior for Numerical Calculations by the Euler/Lagrange Method for Strongly Coupled Phases." American Society of Mechanical Engineers, Fluids Engineering Division, Vol. 185, 1994, pp. 191–202.

[32] Crowe, C. T., Troutt, T. R., and Chung, J. N., "Numerical Models for Two-Phase Turbulent Flows," *Annual Review of Fluid Mechanics*, Vol. 28, 1996, pp. 11–43. doi:10.1146/annurev.fl.28.010196.000303

[33] Smiljanovski, V., and Brehm, N., "CFD Liquid Spray Combustion Analysis of a Single Annular Gas Turbine Combustor," ASME Paper 99-GT-300, 1999.

[34] Chrigui, M., Schroth, G., Sadiki, A., and Janicka, J., "Numerical Prediction of Coal Particles Evolution Behavior in Swirled Flow with and Without Combustion Using an Euler–Lagrangian Coupling," Fifth International Symposium on Coal Combustion (ISCC), Nanjing, China, 2003.

[35] Schäfer, M., *Numerik im Maschinenbau*, Springer–Verlag, Berlin, 1999.

[36] Kenny, R. J., Hulka, J. R., Moser, M. D., and Rhys, N. O., "Effect of Chamber Backpressure on Swirl Injector Fluid Mechanics," *Journal of Propulsion and Power*, Vol. 25, No. 4, 2009, pp. 902–913. doi:10.2514/1.38537

[37] Batarseh, F. Z., Gnirss, M., Roisman, I. V., and Tropea, C., "Aerodynamic Instability of a Spray Generated by an Airblast Atomizer," *Proceedings of the 21st ILASS-Europe Meeting*, Mugla, Turkey, Sept. 2007.

K. Frendi
Associate Editor